Title

Lipid Unsaturation Properties Govern the Sensitivity of Membranes to Photoinduced Oxidative Stress

Journal

Biophysical Journal, 116(5)

ISSN

0006-3495

Authors

Bour, Aurélien
Kruglik, Sergei G
Chabanon, Morgan
et al.

Publication Date

2019-03-01

DOI

10.1016/j.bpj.2019.01.033

Peer reviewed

Biophysical Journal
Article

Biophysical Society

Lipid Unsaturation Properties Govern the Sensitivity of Membranes to Photoinduced Oxidative Stress

Aurélien Bour,[1] Sergei G. Kruglik,[1] Morgan Chabanon,[2] Padmini Rangamani,[2] Nicolas Puff,[3,4] and Stephanie Bonneau[1,*]

[1]Sorbonne Université, Faculté des Sciences et Ingénierie, CNRS, Laboratoire Jean Perrin, Paris, France; [2]Department of Mechanical and Aerospace Engineering, University of California San Diego, La Jolla, California; [3]Sorbonne Université, Faculté des Sciences et Ingénierie, UFR 925, Paris, France; and [4]University Paris Diderot, Sorbonne Paris Cité, CNRS, Laboratoire Matière et Systèmes Complexes, UMR 7057, Paris, France

ABSTRACT Unsaturated lipid oxidation is a fundamental process involved in different aspects of cellular bioenergetics; dysregulation of lipid oxidation is often associated with cell aging and death. To study how lipid oxidation affects membrane biophysics, we used a chlorin photosensitizer to oxidize vesicles of various lipid compositions and degrees of unsaturation in a controlled manner. We observed different shape transitions that can be interpreted as an increase in the area of the targeted membrane followed by a decrease. These area modifications induced by the chemical modification of the membrane upon oxidation were followed in situ by Raman tweezers microspectroscopy. We found that the membrane area increase corresponds to the lipids' peroxidation and is initiated by the delocalization of the targeted double bonds in the tails of the lipids. The subsequent decrease of membrane area can be explained by the formation of cleaved secondary products. As a result of these area changes, we observe vesicle permeabilization after a time lag that is characterized in relation with the level of unsaturation. The evolution of photosensitized vesicle radius was measured and yields an estimation of the mechanical changes of the membrane over oxidation time. The membrane is both weakened and permeabilized by the oxidation. Interestingly, the effect of unsaturation level on the dynamics of vesicles undergoing photooxidation is not trivial and thus carefully discussed. Our findings shed light on the fundamental dynamic mechanisms underlying the oxidation of lipid membranes and highlight the role of unsaturations on their physical and chemical properties.

INTRODUCTION

Aerobic metabolism in cells relies on the oxidation of organic compounds such as fatty acids, allowing cells to produce energy. However, the phospholipids that constitute cell membranes are also sensitive to oxidative stress, which can lead to membrane damage, aging, and potentially cell death (1–3). The molecular processes responsible for the oxidation of unsaturated lipids involve the chemical modification of their double bonds and potential cleavage of the lipid chains (4,5). Therefore, it is essential to consider the degree of unsaturation of fatty acids to understand the mechanisms allowing lipid membranes to withstand oxidative stress.

Biological membranes contain large amounts of mono- and polyunsaturated fatty acids, as well as traces of transition metals necessary for oxidative reactions. As they are constantly subjected to oxidation—in particular because of the respiratory chain—cellular membranes suffer from a variety of irreversible damages. Their oxidative state is defined as the balance between oxidant and antioxidant species, an imbalanced situation leading sequentially to stages of oxidative stress, cytotoxicity, and pathological states (6,7). Oxidative stress is known to be involved in cell aging and, if uncontrolled, in a variety of diseases including Parkinson's and Alzheimer's neurodegenerations and cancer (8–13). Oxidation-induced changes in membranes properties, such as fluidity and permeability (14–16), can result in abnormal and dysfunctional protein assemblies and in the leakage of vital molecules from organelles. Therefore, understanding membrane behavior with respect to their lipid unsaturation degree is an important biomedical challenge.

The first step of unsaturated lipid oxidation leads to the formation of hydroperoxides through a chain reaction ending when two lipid radicals react together (4,5). Because of their polarity, the peroxidized hydrocarbon tails are thought to migrate to the lipid-water interface, which increases the molecule area and changes the packing parameter (17–19). The second step consists of further oxidation

Submitted September 12, 2018, and accepted for publication January 29, 2019.

*Correspondence: stephanie.bonneau@sorbonne-universite.fr

Editor: Kalina Hristova.

https://doi.org/10.1016/j.bpj.2019.01.033

producing secondary products, including alcohols, ketones, alkanes, aldehydes, and ethers (20,21). These products are used as an index of lipid oxidation, mainly to estimate the oxidation level of complex biological systems (22). The resulting cleaved lipids have a conical shape with a larger head/tail surface area ratio and tend to increase the membrane permeability to solutes such as sucrose and glucose (23).

An effective and controlled way to induce oxidation processes in a system is to use photosensitizers to generate reactive oxygen species (ROSs) upon light irradiation (24). Known as the photodynamic effect, the photochemical induction of oxidation is also involved in ultraviolet cytotoxicity and light-related aging on tissues containing endogenous porphyrins (25). Moreover, together with the preferential retention of certain photosensitizers by tumors as compared to normal surrounding tissues (26), such photoinduced cytotoxicity has been applied as an antitumoral therapy known as the photodynamic therapy (27).

Simplified models of biological membranes such as lipid vesicles are powerful tools for investigating how photoinduced oxidative species impact the phospholipid bilayer. Lipid vesicles exposed to photooxidation have been shown to exhibit a two-step behavior, corresponding to a sequential increase and decrease in membrane surface area. These modifications induce vesicle fluctuations and shape transitions (28–31), accompanied by modifications in the membrane viscosity (32), bending modulus (33), area expansion modulus (34), and permeability (28,29,35,36). Similar effects have also been reported in polymersomes (37). Although correlations with chemical mechanisms have been proposed (30), the underlying dynamic chemical scenario remains largely unexplored because of a lack of in situ measurement during the oxidation process.

In this article, we investigate how lipid oxidation affects the dynamic behavior of artificial membrane models. We use giant unilamellar vesicles (GUVs) made of controlled lipid composition with various degrees of unsaturation and expose them to photooxidation by light activation of chlorin e6 photosensitizer (Ce6, Fig. 1). Special attention is given to the number and position of lipid unsaturations. We first describe the time evolution of GUV morphology upon photooxidation and relate it to the membrane permeabilization. Then, we use Raman microspectroscopy combined with optical tweezers to follow in situ the membrane chemical modifications of vesicles in an aqueous environment. These results are discussed in relation to the observed mechanical and morphological changes.

MATERIALS AND METHODS

Chemicals

All chemicals were purchased from Sigma (St. Louis, MO), except the lipids (Fig. 1) 1,2-dilinolenoyl-*sn*-glycero-3-phosphatidylcholine (C18:3-PC), 1,2-dilinoleoyl-*sn*-glycero-3-phosphatidylcholine (C18:2, DLPC), 1,2-dioleoyl-*sn*-glycero-3-phosphatidylcholine (C18:1, DOPC), 1,2-dipetroselenoyl-*sn*-glycero-3-phosphatidylcholine (DOPC-$\Delta 6$), 1,2-dielaidoyl-*sn*-glycero-3-phosphatidylcholine (DOPC-*trans*), and 1,2-dimyristoyl-*sn*-glycero-3-phosphatidylcholine (C14:0, DMPC) from Avanti Polar Lipids (Alabaster, AL) and Ce6 from Frontier Scientific (Logan, UT). The lipids were handled very carefully, in vaccuum or under nitrogen atmosphere when possible. For all lipids, the absence of oxidation is measured by Raman (spectra at $t = 0$). Chlorin stock solution (5 mM) was prepared in ethanol and kept at $-18°C$. The experimental Ce6 aqueous solutions were prepared and used without delay and handled in the dark. The osmolarity of the solutions was checked with an osmometer (Löser Messtechnik, Berlin, Germany).

Vesicle formation

The lipids (C18:3-PC, DLPC, DOPC, DOPC-*trans*, or DOPC-$\Delta 6$) were solubilized in chloroform. For the determination of the binding constant

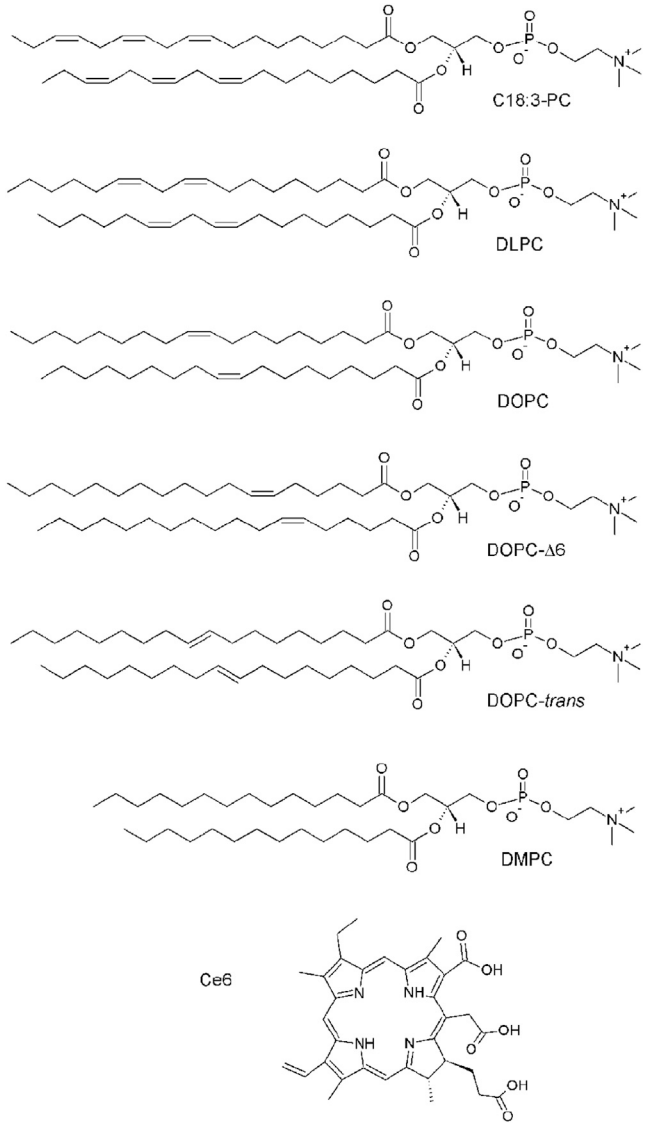

FIGURE 1 Formulae and abbreviations of the lipids composing the various GUVs, as well as of the photosensitizer Ce6.

between lipid membranes and Ce6, large unilamellar vesicles (LUVs) were prepared by the extrusion method (38). After evaporation of chloroform, lipids were dispersed in phosphate-buffered saline buffer by vortexing. Using an extruder device (Avanti Polar Lipids), the liposome suspension was extruded 8–10 times through a polycarbonate membrane filter (Poretics, Livermore, CA) with pores of 200 nm.

The electroplating method (39) was used to form GUVs with diameters of 20–30 μm. Lipid mixtures in chloroform were deposited on indium tin oxide-covered glass plates, and chloroform was evaporated in vacuum. A formation chamber was then made from two such glass plates and a Teflon spacer of 4 mm. The chamber was then filled with a solution of 300 mM sucrose and HEPES buffer solution (2 mL (pH 7.8) HEPES 0.5 mM). An alternative current field of 1 V and 8 Hz was applied between the plates for 4 h. For experiments, the GUVs were mixed with a ~300 mM glucose solution made in the same buffer. The solution carefully adjusted ~5 mOsm/L higher than the external sucrose solution to limit the strain of the membrane. The density difference between sucrose and glucose caused the GUVs to sediment to the bottom of the chamber. The difference in optical index between sucrose inside and glucose outside the vesicle allowed phase contrast microscopy observations.

Measurements of the Ce6 affinity to membranes

For the steady-state study of the interaction between the Ce6 lipid membranes of various compositions, fluorescence spectra were measured with an Aminco Bowman Series 2 spectrofluorimeter (Edison, NJ). All experiments were done in triplicates. LUV solutions were prepared at different concentrations of lipids, and 10 μL of 10 μM Ce6 solution was added to 2 mL of each vesicle preparation. The fluorescence spectra were recorded 2 min after the sample preparation. Data thus obtained were analyzed as described elsewhere (28,40,41). The fluorescence intensity at a wavelength corresponding to the maximum of fluorescence emission of Ce6 incorporated into the membrane was plotted as a function of the lipid concentration. The binding constant, K_B, was derived according to the relationship

$$F = F_0 + \frac{(F_\infty - F_0) \times K_B \times [lip]}{1 + K_B \times [lip]}, \qquad (1)$$

where F_0, F_∞, and F are the fluorescence intensities corresponding to zero, total, and intermediate incorporation of Ce6 into vesicles, respectively. Lipid molecules are in large excess, and the bilayer is far from being saturated with Ce6. Therefore, it was assumed that the membrane properties were independent of the number of bound Ce6 molecules and [*lip*] was equal to the total lipid concentration.

Partition experiments were carried out with an excitation wavelength at 410 nm. Upon the addition of vesicles, the intensity of the fluorescence emission increases significantly and shifts from 660 to 668 nm. Typical fluorescence emission spectra of the photosensitizer in solution and in the presence of various DLPC lipid concentrations are shown in Fig. 2 (*inset*). These spectral changes are characteristic of the transfer of the chlorin from an aqueous to a hydrophobic environment (28,36,40,42). The plot of the fluorescence intensity at 668 nm versus the lipid concentration shows a saturation profile (see Fig. 2). The binding constant value, K_B, was determined by fitting the experimental data with Eq. 1 and is reported in Table 1. The obtained values are in good agreement with previous data obtained (28,36) and depend on the membrane composition. Such an effect has been previously observed for the interactions of photosensitizers with various membranes (26,28,37,40,42).

Labeling of GUVs

GUVs were labeled with Ce6 as previously reported (28,29). The Ce6 concentration used was calculated according to the K_B value determined beforehand for each lipid mixture to ensure an identical membrane labeling.

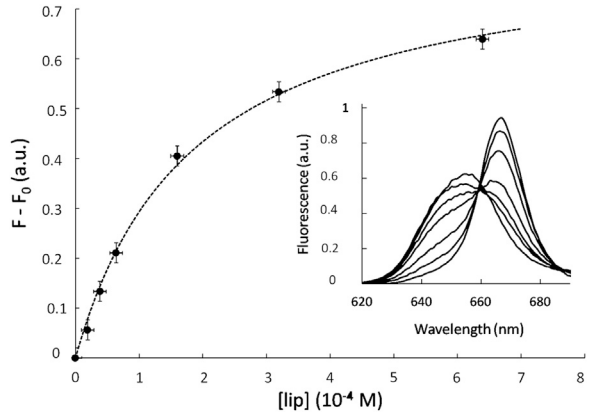

FIGURE 2 Incorporation of Ce6 within lipid membranes. Evolution of the Ce6 fluorescence emission upon incorporation into vesicles (here, made with pure DLPC; Ce6 concentration is 5×10^{-8} M) is shown. The excitation wavelength is 410 nm, and the fluorescence intensity is recorded at 668 nm. Equation 1 is used to fit experimental data and yields the binding constant K_B. The inset shows the red shift of Ce6 fluorescence peak upon incorporation within the membrane.

The homogeneous distribution of the fluorescent Ce6 molecules within the vesicle membranes was assessed by fluorescence microscopy.

Observation and illumination

GUVs were observed under an inverted microscope (Nikon Eclipse TE 300 DV) equipped with a high numerical aperture phase oil objective (CFI Plan apochromat DM 60 numerical aperture: 1.4; Nikon, Champigny-sur-Marne, France). Illumination was provided by a 120 W metal halide lamp with a 405 ± 10 nm bandpass filter. Neutral density filters (ND × 8) were used to reduce illumination level. GUVs were simultaneously imaged in bright-field using the halogen lamp of the microscope, and the fluorescence of Ce6 was cut off by using an appropriate filter. Image acquisition (100 ms integration time) was performed with a CCD camera (Neo sCMOS; Andor Technology, Belfast, UK). The acquisition, processing, and image analysis were performed with NIS-Element provided by Nikon and ImageJ (National Institutes of Health, Bethesda, MD). For each membrane composition, the images of at least 20 vesicles from three sample preparations were analyzed separately. The intratrial variability is reported in the Supporting Materials and Methods. When photooxidizing the membrane, illumination was kept constant from the initial time.

Chemical scenario

To monitor the chemistry of lipid oxidation, Raman spectra of corresponding lipid vesicles in the presence of photosensitizer Ce6 were recorded using a home-built Raman tweezers microspectroscopy (RTM) setup described elsewhere (43). Briefly, RTM technique combines optical trapping (44) with Raman probing: the same laser radiation is used for both optical trapping of the vesicles and excitation of Raman scattering from the vesicles' constituent biomolecules. The light at 780 nm is provided by a continuous-wave Ti:Sapphire laser (model 3900S; Spectra Physics, Santa Clara, CA) pumped by an argon-ion laser (Spectra Physics Stabilite 2017; Spectra Physics). The laser beam is focused by a water-immersion infinity-corrected objective (LUMFL 60×, NA 1.1; Olympus, Tokyo, Japan) brought into contact with a droplet (~100 μL) of water buffer containing the vesicles of interest. The laser power was adjusted to ~70 mW inside the sample suspension. LUV concentration was adjusted to ~100 μg/mL in lipids and to ~0.1% in Ce6. Our RTM setup employs

upright microscope configuration, and the same objective is used to collect Raman signal in a back-scattering geometry and to deliver it into a spectrograph (Acton SpectraPro 2550i) coupled with a deep-depleted back-illuminated near infra red CCD (SPEC-10 400BR/LN; Princeton Instruments, Trenton, NJ). Raman light is focused onto the spectrograph's entrance slit (semiconfocal configuration, slit width 50 μm) by an achromatic lens with $f = 75$ mm. The Raman signal is spectrally separated by two Semrock RazorEdge long-pass filters (grade U; Semrock, Rochester, NY): one (blocking filter) with the edge wavelength of 780 nm is placed normally to the optical beam just before the focusing lens, and another one with the edge wavelength of 830 nm is used as a dichroic beam splitter at an angle of incidence 45°; it reflects laser light at 780 nm and transmits all the wavelengths longer than 785 nm. Spectral resolution in all Raman experiments was $\sim$5 cm^{-1}. Frequency calibration was performed using Raman lines of toluene with ± 2 cm^{-1} absolute accuracy and relative frequency position accuracy better than ± 1 cm^{-1}.

All experiments were done in triplicates. Raman spectra were continuously acquired every 3 s within 10-min intervals using WinSpec software; further data treatment was performed using IgorPro for Windows software. The informative signal from the vesicles in the sample volume arises as additional spectral features appear on top of the water buffer Raman spectrum, as soon as the vesicles are trapped at the focus of the laser beam. Simultaneously with the event of vesicles trapping, the sample droplet was illuminated by weak light at 405 nm from the microscope white-light illumination system passing through the bandpass interference filter (405 $\pm$ 5 nm; Andover, Salem, NH) to initiate the photosensitizing effect. The details of raw Raman spectra treatment were described in detail elsewhere (43). In this study, each spectrum is the mean of three acquisitions. For Raman kinetics evaluation based on spectral band areas, an additional step of spectra treatment was introduced, consisting of automatic background correction using linear functions and spectra normalization on ν(C-N+) stretch of polar heads.

RESULTS AND DISCUSSION

Preparation of the photooxidable vesicles

To investigate the effect of lipid unsaturation on membranes undergoing photooxidation, we use electroformed GUVs made of five distinct compositions. To vary the level of membrane unsaturation we considered 1) 18:1 GUVs, made of pure monounsaturated lipid DOPC; 2) 18:2 GUVs, composed of pure polyunsaturated lipid DLPC; and 3) 18:1/18:3 GUVs, a mixture of C18:3-PC and DOPC at 50/50 molar ratio that has a mean level of unsaturation similar to DLPC. Then, to address the role of the geometry of the unsaturation, we used 4) 18:1 *trans*-GUVs composed of DOPC-*trans* lipids and 5) 18:1 Δ6-GUVs made of DOPC-Δ6 lipids. All unsaturated lipids used here were C18-PC to address the effects of the unsaturation of the lipid tails and not that of their headgroup, nature, or length. Control experiments were carried out using GUVs made of the saturated lipid DMPC. In all cases, the photosensitizer Ce6 was added to the GUV membranes to enable the photo control of the membrane oxidation. Beforehand, partition experiments were carried out to quantify the propensity of the Ce6 to insert within the various membranes and determine the suitable Ce6 concentration for each membrane composition (see binding constants in Table 1).

TABLE 1 Lipid Content and Ce6 Binding Constants for Each Type of Model Vesicle

Model Vesicles	Lipid Content	K_B (M^{-1})
18:1 GUVs	DOPC	$(5.00 \pm 1.4) \times 10^3$
18:2 GUVs	DLPC	$(6.83 \pm 0.20) \times 10^3$
18:1/18:3 GUVs	DOPC/C18:3-PC (50/50 mol/mol)	$(4.61 \pm 0.11) \times 10^3$
18:1 Δ6-GUVs	DOPCΔ6	$(5.36 \pm 0.13) \times 10^3$
18:1 *trans*-GUVs	DOPC-*trans*	$(3.25 \pm 0.5) \times 10^3$
DMPC GUVs	DMPC	$(6.1 \pm 0.6) \times 10^3$

The GUVs were prepared in a solution of sucrose and diluted in a glucose solution to produce a difference in optical index between the inner sucrose and outer glucose solutions, facilitating observations and measurements by phase contrast microscopy. GUVs were observed by bright-field optical microscopy, and photooxidation was induced by illumination with a 120 W metal halide lamp with a 405 $\pm$ 10 nm bandpass filter.

Morphological evolution of GUVs under photooxidation

In the absence of irradiation, all GUVs appeared spherical, although slightly floppy because of the small osmolarity mismatch between the inner and outer solutions (5 mOsm/L; see Materials and Methods for details). As seen from Fig. 3, upon illumination, the Ce6-labeled GUVs exhibited a dynamic morphology characterized by two consecutive stages: first, a transient shape destabilization with the appearance of outward buds or membrane invaginations (stage 1), followed by recovery of a spherical shape accompanied by a progressive decrease in optical contrast and, in certain cases, a reduction in vesicle size (stage 2). In comparison, control vesicles either containing no Ce6 or lacking unsaturations (DMPC GUVs labeled with Ce6) showed no shape changes upon illumination, confirming that the observed dynamics is solely induced by the oxidation of unsaturated lipids through the photosensitizer Ce6.

The shape transitions observed in stage 1 are consistent with reported dynamics of lipid vesicles of various composition containing different photosensitizers such as chlorins, fluorescent probes or methylene blue (28–31,34). The shape destabilization is attributed to a transient increase in membrane area, possibly coupled to a softening of the lipid bilayer mechanical properties. Most importantly, we find that the kinetics of shape transition is strongly dependent on the unsaturation properties of the membrane lipids. Although the duration of stage 1 is om the order of 10 s for both 18:1 GUVs and 18:2 GUVs, it is decreased to $\sim$2 s for 18:1/18:3 GUVs. For 18:1 Δ6-GUVs, whose double bond is nearest the lipid head, stage 1 lasts for up to 30 s and presents shape fluctuations of higher amplitudes. In contrast, 18:1 *trans*-GUVs seem unaffected and retain their

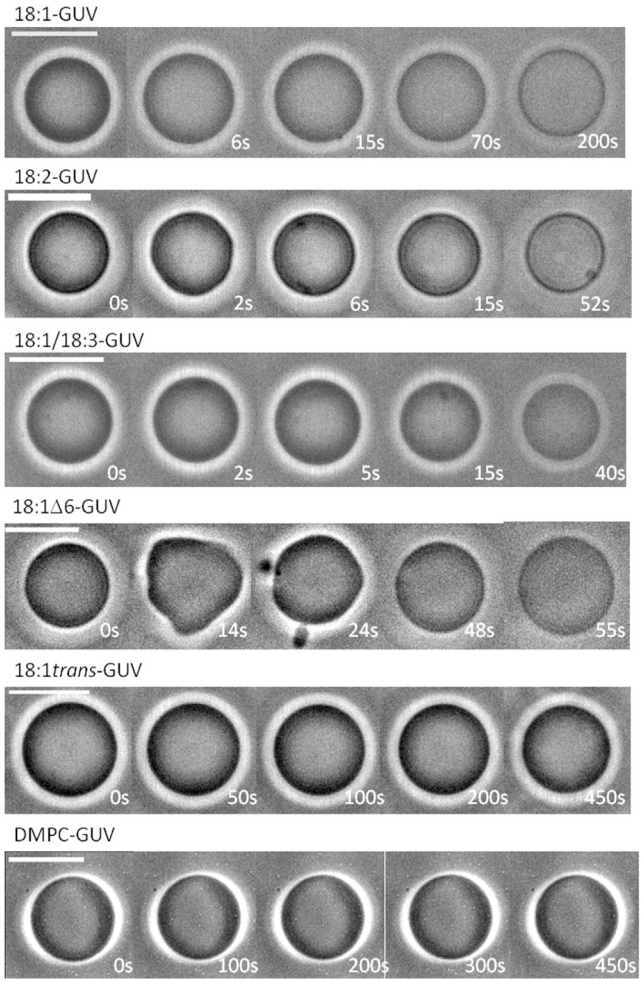

FIGURE 3 Effect of lipid unsaturation on the morphological evolution of GUVs under photooxidation: morphological changes of Ce6-labeled GUVs of various compositions exposed to photooxidation. Shortly after irradiation, GUVs enter a first stage characterized by an increase of membrane surface area, leading to shape destabilization. Then, during a second stage, a decrease of membrane area allows the GUVs to recover a spherical shape, concomitant with a loss of contrast. Irradiation starts at time $t = 0$ s, and the timescale is adjusted according to the duration of the processes, i.e., the composition of the vesicles. The figure presents images of vesicles of comparable radii ($\sim$5 μm); the intratrial variability, related to the system size, is presented in the Supporting Materials and Methods. Scale bars, 10 μm. To see this figure in color, go online.

spherical shape, initial radius, and optical contrast for the entire duration of the experiment (450 s).

Pulsatile dynamics of photooxidized vesicles

To quantitatively compare the effects of lipid unsaturation on the dynamics of GUVs undergoing photooxidation, we recorded for each vesicle composition the time evolution of 1) their optical contrast and 2) their radius. As seen in Fig. 4, all photosensitive GUVs showed a dramatic decrease in optical contrast during stage 2. Given that the optical contrast is the result of the difference in sugar composition between the interior (sucrose) and exterior (glucose) of the GUVs, the decrease in contrasts is interpreted as a combined effect of the dilution and leak-out of encapsulated sucrose due to a progressive permeabilization of the lipid membrane.

Strikingly, the vesicle radii exhibited an overall decrease, marked by pulsatile behavior of progressive swelling and abrupt drop for 18:1 GUVs, 18:2 GUVs, and 18:1/18:3 GUVs. This dynamics is similar to those of lipid GUVs undergoing swell-burst cycles induced by osmotic stress (45–47) or subject to surfactants (48,49). Based on these observations, we propose the following mechanism for the GUVs' dynamics (Fig. 5). Upon illumination, the Ce6-labeled GUVs generate ROSs that lead to oxidative reactions of the unsaturated lipid tails. At short timescales ($\sim$10 s), the oxidation produces an increase in membrane area, resulting in shape destabilization of the initially spherical vesicles (stage 1) (30). At longer timescales, the surface area of photooxidized membranes progressively reduces, resulting in a recovery of the spherical shape followed by a decrease in the GUV volume (stage 2). Concomitantly, oxidative products are released from the membrane both in the intravesicular space and in the surrounding bath. However, because the volume of the bath is much larger than the vesicle volume, a positive concentration difference builds up between the inside and the outside of the GUV. Because the permeability of the membrane to oxidative product is negligible when compared to its permeability to water, the concentration difference induces a hypotonic stress, driving an inflow of water through the membrane and the progressive swelling of the GUV. Lipid membranes are elastic materials able to withstand $\sim$4% surface strain before rupturing (50). Once this critical strain is reached, the GUV opens a micrometer-sized pore through which the inner solution leaks out, relaxing the internal pressure and decreasing in turn the vesicle volume and membrane tension. This in turn allows for the pore line tension—induced by the hydrophobic lipid mismatch at the pore edge—to drive the resealing of the pore (47). This swelling and bursting sequence is repeated in successive cycles as long as oxidative species are released from the membrane. The 18:1 Δ6-GUVs showed a slightly different behavior, with no clear swell-burst cycles, although these may happen with amplitudes smaller than our setup can detect.

To confirm that the swell-burst cycles occurred in 18:1 GUVs, 18:2 GUVs, and 18:1/18:3 GUVs, we tracked the vesicles with rapid video microscopy (100 Hz) in search of a transient pore opening. As shown in Fig. 6, we observed short-lived pore opening up to a few microns in radius for $\sim$50 ms, thus confirming the proposed swell-burst mechanism. We then calculated for each cycle the maximal area strain (Fig. 7, *A–D*). For the GUVs for which pore openings have been demonstrated, this corresponds to the critical strain ε_c at which membrane bursts.

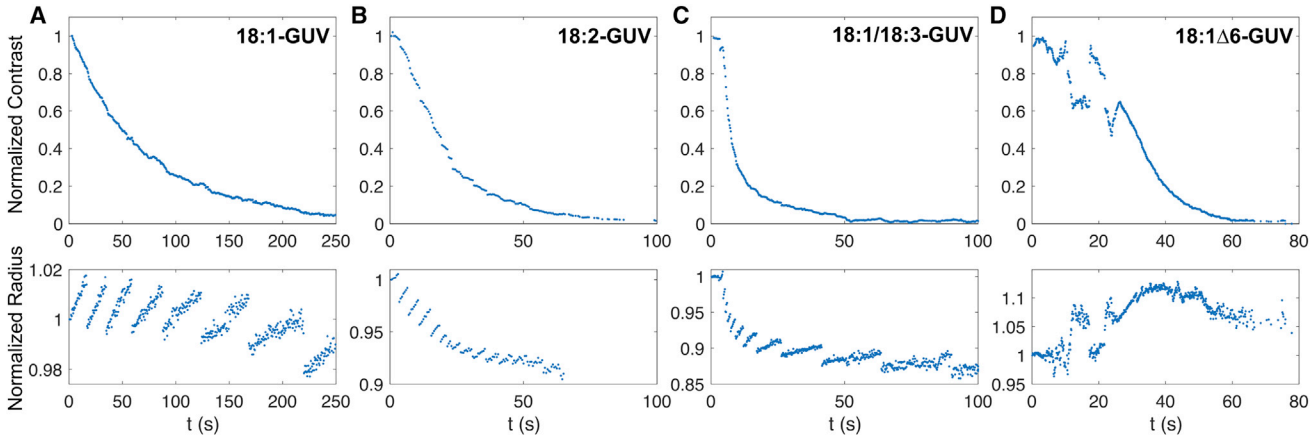

FIGURE 4 Time evolution of optical contrast and radius of GUVs undergoing photooxidation. (*A*) 18:1-GUV; (*B*) 18:2-GUV; (*C*) 18:1/18:3-GUV; (D) 18:1Δ6. (*Top*) Evolution of the contrast between the inside and the outside of the oxidized vesicles is shown. The decay is the result of a decrease in concentration difference between the GUVs inner sucrose solution and the surrounding glucose solution. (*Bottom*) Vesicle radii exhibit cycles of progressive increases followed by abrupt drops, characteristic of GUV swell-burst cycles. The results presented are those of the same vesicles as those in Fig. 3. To see this figure in color, go online.

For 18:1 GUVs and 18:2 GUVs, the maximal strain decreases with each cycle, reaching a final value about four times lower than at the beginning of stage 2: ε_c is decreased, respectively, for 18:1 GUVs and 18:2 GUVs from (6.61 $\pm$ 2.07) and (3.5 $\pm$ 1.00)% down to (1.48 $\pm$ 0.47) and (1.3 $\pm$ 0.5)%. This decrease suggests a weakening of the membranes undergoing oxidation. In contrast, for 18:1/18:3 GUVs, the maximal strain stays around 3%, with a slight increase within the range of the statistical errors.

Contribution of membrane permeabilization to GUV contrast decay

From our observations of transient pores (Fig. 6), we did not find any significant drop in vesicle contrast with pore opening, suggesting that the short times of the pore opening events do not allow diffusion through the pore to affect the concentration imbalance in sucrose and glucose. Indeed, convection-driven leak-out alone does not change the concentration of sucrose inside the vesicle (47). Therefore, the main mechanisms leading to the progressive loss in contrast observed in Fig. 3 are the dilution of the inner content by the osmotic influx of water, as well as the permeabilization of the membrane to sucrose upon oxidation, in accordance with the packing defect and/or pre-pore-opening scenarios, in which the evolution of hydrophobic defects of the membrane involve local increase in spacing of lipid molecules (28,29,35,51,52).

To evaluate the permeabilization of the lipid membrane by photooxidation, we propose a mathematical model of

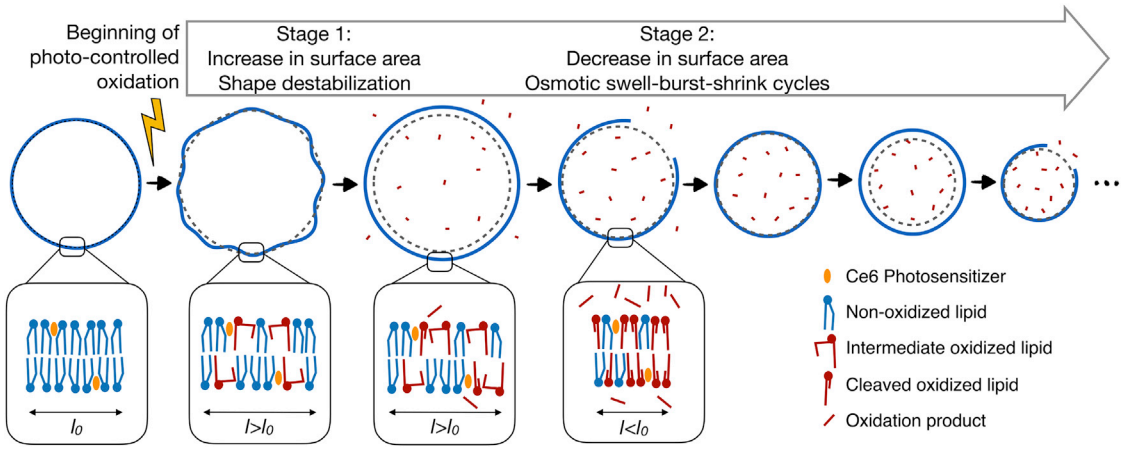

FIGURE 5 Sketch of the proposed mechanism involved in the dynamics of the vesicles over oxidation. To see this figure in color, go online.

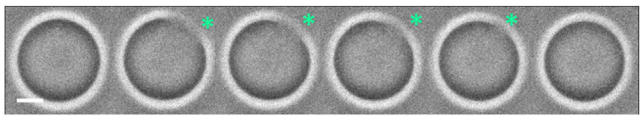

FIGURE 6 Time evolution of a transient pore opening in an 18:2 GUV under photooxidation. The pore is marked with an asterisk. Frequency of image acquisition: 100 Hz. Scale bars, 10 μm. To see this figure in color, go online.

the swell-burst process (see Supporting Materials and Methods for full derivation). Based on this framework, we estimate the time evolution of the intravesicular sucrose concentration (c_s) during a given cycle (n):

$$\frac{dc_s}{dt} \simeq \frac{-3}{R_{0n}}\left(P_s + \frac{\Delta R_n}{\Delta t_n}\right)c_s, \tag{2}$$

where R_{0n} is the initial vesicle radius of the n^{th} cycle, P_s is the membrane permeability to sucrose, ΔR_n is the total amplitude of the vesicle radius during that particular cycle, and Δt_n is the cycle period. This equation states that the sucrose concentration in the vesicle can decrease either by permeating through the membrane (first term in parenthesis) or by dilution when the influx of water increases the vesicle volume (second term in the parenthesis). Assuming that the membrane permeability to sucrose is constant within the period of a cycle, the solution of Eq. 2 is an exponential decay of the form

$$c_s(t) = c_s(t_{0n})e^{-(t-t_{0n})/\tau}, \tag{3}$$

where t_{0n} is the time at which the cycle starts and τ is the characteristic decay time of the sucrose concentration, defined as

$$\tau = R_{0n}\Big/\left[3\left(P_s + \frac{\Delta R_n}{\Delta t_n}\right)\right]. \tag{4}$$

The two terms in the denominator of Eq. 4 reflect the two processes involved in the progressive loss of contrast of the vesicles, i.e., the permeabilization of the membrane to the sucrose and the osmotic influx of water, respectively. For each GUV cycle, the measured quantities are ΔR_n, Δt_n, R_{0n}, and t_{0n}. Therefore, assuming that the optical contrast is proportional to the sucrose concentration in the GUVs, one can determine P_s, the membrane permeability to sucrose, by obtaining τ from the fit of Eq. 3 to the contrast decay during a given cycle. $\Delta R_n/\Delta t_n$ is directly derived from the radii measurements (Fig. 3). We observed that the magnitude of this term represents less than 20% of P_s for 85% of the cycles and that its contribution decreases along the permeabilization (see Fig. 7, *E–L*). Therefore, the loss of contrast observed in Fig. 4 is essentially governed by the permeabilization of the membrane to the sucrose.

Moreover, except for 18:1/18:3 GUVs, we did not find evidence of any important variation in membrane permeability over the oxidation time (Fig. 7), suggesting that the oxidation of the membrane induces an increase of its permeability to sucrose in an abrupt manner by three orders of magnitude, a native phospholipid membrane being almost

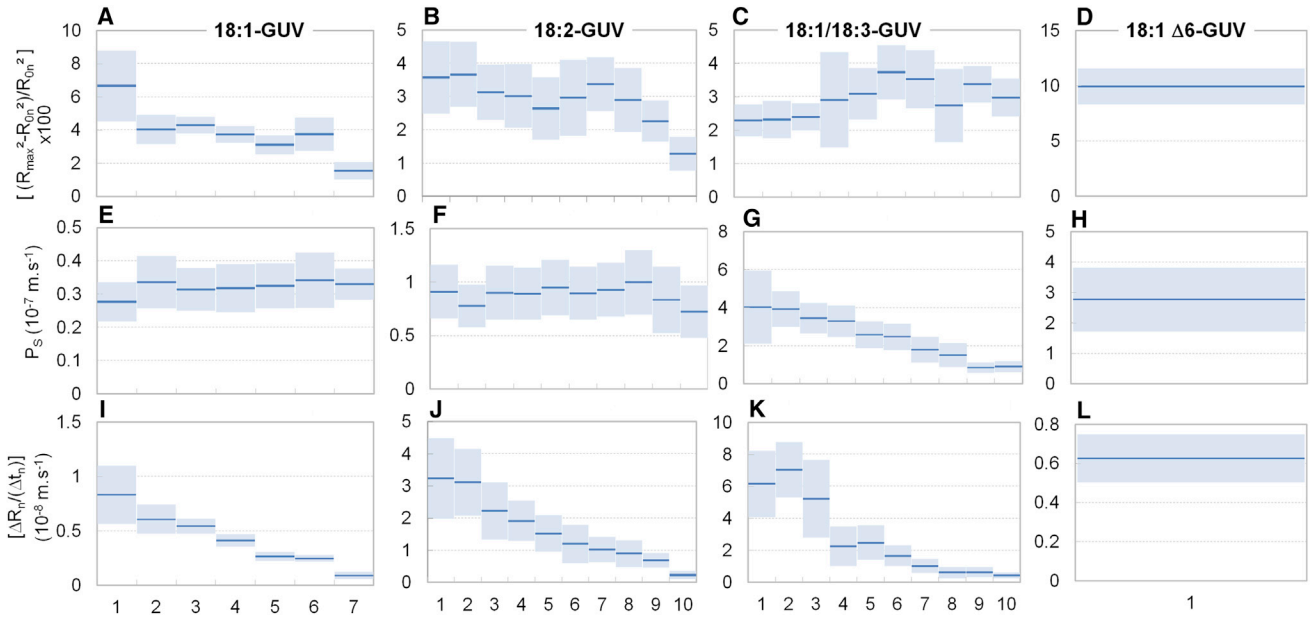

FIGURE 7 Evolution of physical parameters of GUVs undergoing photooxidation as a function of the swell-burst cycle number. (*A–D*) Evolution of the membrane critical strain, $R^2_{max} - R^2_{0n}/R^2_{0n}$. (*E–H*) Permeability to sucrose, *Ps*. (*I–L*) Progressive decrease of the water influx related term of Eq. 4, $\Delta R_n/\Delta t_n$. The 18:1 Δ6-GUVs are analyzed as if they were undergoing a unique cycle. Dark lines are the mean of 20 vesicles per compositions, error bars are $\pm$ SDs. To see this figure in color, go online.

impermeable to sucrose ($P_s^* = \sim 10^{-12}$–10^{-10} m/s). Interestingly, such an observation suggests a threshold effect between two distinct permeability regimes for native and oxidized membranes, regardless of their oxidation degree and the level of oxidized products (16). So, the GUVs contrast decay is characterized by two parameters: t_0, the time of onset of contrast decay, and P_s, the permeability to sucrose of oxidized membranes, on which the characteristic decay time essentially depends. The measured values of t_0 for 18:1 GUVs and 18:2 GUVs (9.4 ± 4.5 and 10.1 ± 5.1 s, respectively) do not show significant differences. This indicates that the onset of the membrane permeabilization is independent of the number of double bonds in the lipid tail. However, the t_0 obtained for 18:1 Δ6-GUVs is 28.4 ± 5.5 s, threefold higher than 18:1 GUVs and 18:2 GUVs, suggesting that the position of the unsaturation determines the initial permeability resistance to photooxidation. For 18:1/18:3 GUVs, t_0 value is 2.6 ± 0.8 s, fourfold smaller than for 18:1 GUVs, revealing the weak stability of this membrane upon oxidation.

In contrast, the value of P_s (Fig. 7, *E–H*) of oxidized membranes increases with the number of unsaturation from (0.32 ± 0.02) × 10^{-7} ms^{-1} for 18:1 GUVs to (0.87 ± 0.08) × 10^{-7} ms^{-1} for 18:2 GUVs. This behavior indicates a direct correlation between the number of double bounds and the oxidized membrane permeability. For 18:1/18:3 GUVs, after the abrupt increase in the value of P_s compared to that of nonoxidized membranes, we observe throughout stage 2 a decrease of permeability to sucrose from (3.87 ± 0.89) × 10^{-7} ms^{-1} to (0.88 ± 0.24) × 10^{-7} ms^{-1}, a value on the same order of magnitude as for 18:2 GUVs but that remains larger than for the unoxidized membrane. This suggests a reorganization in the lipid membrane, in parallel with its oxidation, possibly involving changes of the structural or dynamics properties such as lipid packing and order (53,54). The fastest loss of contrast occurs for the 18:1 Δ6-GUV, with a P_s value of (1.79 ± 0.81) × 10^{-7} ms^{-1}, showing an oxidation dependence at the position of the unsaturation.

Chemical dynamics of membrane photooxidation

The above analysis gives valuable insight into the mechanical and transport properties of the various GUVs undergoing photooxidation. Yet, the underlying chemical scenario is largely unexplored. Indeed, because reaction intermediates are very short-lived, following the photochemistry involved in membrane alteration in situ is challenging. We used RTM to monitor simultaneously the kinetics of photochemistry involved in LUV oxidation and the morphological response of the vesicles. The main advantage of this technique is that it allows us to follow the dynamics of oxidative cascade in situ. Vesicles labeled with Ce6 were trapped by a strong near infra read light at 780 nm and simultaneously irradiated by a weak near-ultraviolet light at 405 nm to initiate the photo-induced oxidation. The RTM method has been described elsewhere (43,44) and is detailed in the Supporting Materials and Methods. The changes in the Raman spectra of the vesicle lipids were recorded over 10 min, with an accumulation time of 3 s per spectrum effectively determining the time resolution of our RTM kinetic measurements. Raman spectra of Ce6-labeled LUVs composed of unsaturated lipids exhibited bands corresponding to the vibrations of the hydrocarbon chains with some contributions of the polar headgroups (55,56). The assignment of the characteristic Raman bands in spectra of lipid vesicles under study are presented in Table S1. The characteristic photoinduced changes vary depending on the degree of unsaturation. In general, the following processes have been detected and quantified: peroxide formation, through the appearance of a transient Raman band at 840–880 cm^{-1}; C=C bond isomerization, via the appearance of a characteristic derivative-like feature at 1650–1675 cm^{-1} in difference Raman spectra; conjugation of C=C bonds, through the appearance of extra intensity around 1654 cm^{-1}; and a cyclization reaction via the appearance of strong six-membered ring bands at 1000, 1031, and 1596 cm^{-1}. Note that no photoinduced changes were observed for 18:1 *trans*-LUVs.

As shown in Fig. 8, all of the examined vesicles exhibit changes of the bands that were involved in C=C loss or isomerization. All photooxidized lipids also displayed an apparition of a band in the 820–860 cm^{-1} region corresponding to the peroxide apparition, signaled by an increase of the O-OH stretching mode. The oxidation process initiates through the delocalization of the double bonds (C=C), which move along the fatty chain. This results in the formation of *trans* and conjugated double bonds for the mono- and polyunsaturated lipids, respectively. From the kinetics point of view, the rate of C=C attack is directly correlated with the number of unsaturation. Moreover, the isomerization of 18:1 Δ6-LUV is threefold faster than for 18:1 LUV (see Supporting Materials and Methods: the equalization of the *cis* and *trans* C=C bands intensities takes 20 s for DOPC Δ6 vs. 54 s for DOPC). This suggests an important role of the C=C bond position. In parallel to this initial step of double bond delocalization, the peroxidation reaction with oxygen develops, leading to the primary products, the hydroperoxides. The formation of these transient compounds is visible in all spectra except for 18:1 *trans*-GUVs, in which no changes were evidenced. This suggests that the initial delocalization step is necessary for the reaction with oxygen, as attested by the absence of peroxidation of the 18:1 *trans*-vesicles for which the peak at 1670 cm^{-1} remains stable over irradiation time.

Relation between chemical reactions and observed shape transitions

In the presence of oxygen and under light activation, a photosensitizer can lead to two types of oxidative

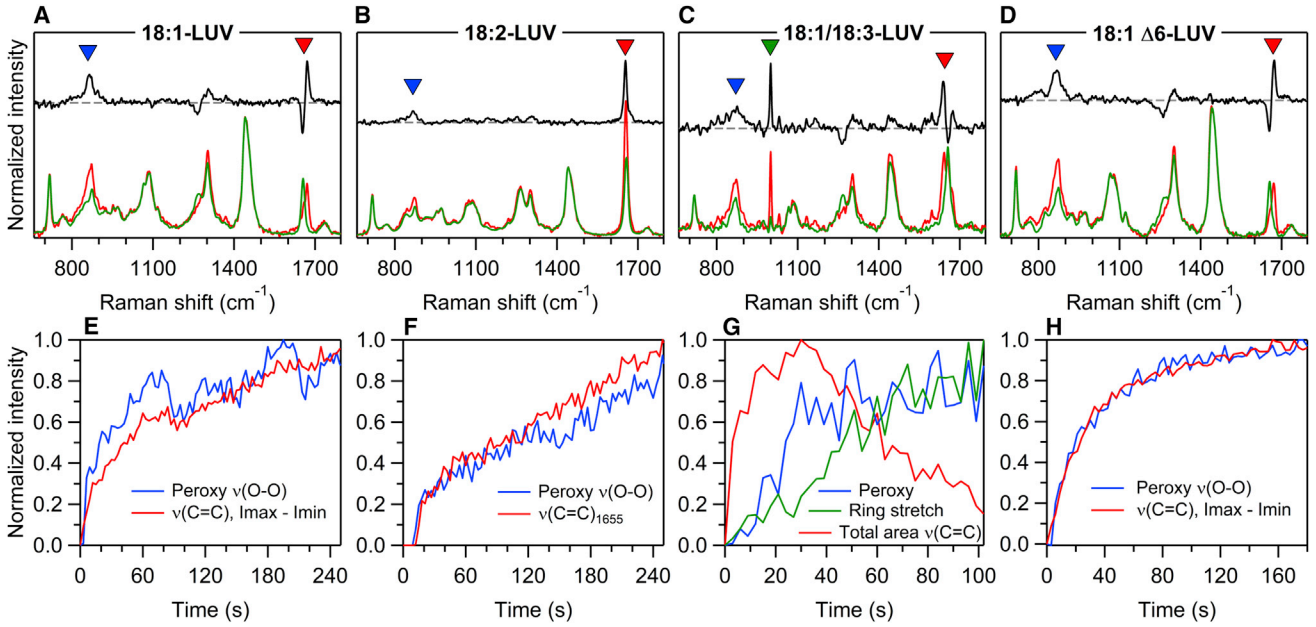

FIGURE 8 Chemical changes during vesicle oxidation. (*A–D*) Raman spectra corresponding to the beginning of the measurements ($t = 0$ s, *green curves*) and to a specific characteristic time (*red curves*, *A*: 165 s, *B*: 216 s, *C*: 51 s, *D*: 60 s). The 1:1 difference spectrum is in black. The characteristic band regions are tagged: peroxy (O-O) stretch (*blue signs*), carbon double-bond stretch (*red signs*), and six-membered ring stretch (*C*, *green signs*). (*E–H*) The Raman kinetics of characteristic band regions is shown. The same colors as for tags in top panel are used: peroxy (O-O) stretch (*blue curves*), carbon double-bond stretch (*red curves*), and six-membered ring stretch (*green curves*).

reactions induced by ROSs. Type I oxidations are initiated by radicals and type II oxidations by singlet oxygen. Because the Ce6 quantum yield is important, the latter process is expected to be dominant in our experiments (32). To determine the oxidative nature of the light-induced membrane responses and to discriminate which chemical mechanism was dominant, we used sodium azide as quencher of singlet oxygen. None of the GUVs formed in 50 mM sodium azide solution showed sign of oxidation upon illumination.

These observations are in agreement with our Raman in situ analysis, highlighting that the lipid tail C=C double bonds are the privileged site of the ROS reactions. The subsequent production of hydroperoxides is manifested by an increase of the Raman peak in the 840–880 cm^{-1} region for all the types of vesicles except *trans*-DOPC and DMPC. The production of such a polar group within the hydrophobic area of the membrane strongly changes the structure of the lipid tail. Because this group tends to migrate near the polar zone of the lipid head, this process tends to increase the membrane surface area, leading to the dynamics observed during stage 1 (Fig. 3) (28,29,34). As expected, these two processes are very fast and temporally correlated for all lipids used in this study. Furthermore, we found that the variation of membrane surface area related to the hydroperoxidation depends on the position on the unsaturation, as seen from the large amplitude of the fluctuations during stage 1 of 18:1 Δ6-GUV photooxidation (Fig. 4). This can be explained by the fact that the 18:1 Δ6-GUV double bound is positioned closer to the headgroup than for the other compositions, facilitating its relocation toward the lipid-water interface in the hydrophilic zone of the membrane (57).

During stage 2 of the vesicles' photooxidation dynamics, various degradation products are produced (20,21) and expelled from the hydrophobic core of the membrane because of their increased hydrophilicity. In consequence, such species are not present in the recorded Raman spectra of immobilized vesicles. However, the decrease in double bonds of the tails can be observed in some experiments. The cleaved lipids produced within the oxidized membrane are known to increase membrane permeability, as observed in our experiments during phase 2 (Fig. 4). They also weaken the membrane. Accordingly, at this stage, the optically trapped vesicles are destabilized and burst, leading to a loss of Raman signal. Moreover, cleaved lipids are known to increase membrane permeability (15,23).

Throughout stage 2, the oxidation of the membrane continues, as highlighted by the successive swell-burst cycles of the vesicles resulting from the accumulation of oxidation products. The membrane composition continually changes over the oxidation. So, it would be expected that the permeability of the membrane would increase with increasing oxidation degree. This is clearly not the case, and after an abrupt increase of P_s corresponding to the initiation of stage 2, P_s remains constant (18:1 and 18:2 GUVs) or even slightly decreases (18:1/18:3 GUVs). This evidences that

the membrane permeability is not directly and quantitatively related to the oxidation level and that more complex phenomena have to be taken into consideration. For example, the asymmetric distribution of oxidative damages across the bilayer has been shown to affect membrane permeability (29,36). Hence, structural or dynamics properties of the membrane can be modulated over oxidation (16,53,58), in addition to possible effects of cleaved tail fragments on the membrane properties (15).

CONCLUSION

In this work, we studied the influence of lipid unsaturation on the dynamics evolution of the physical and chemical properties of GUVs undergoing photooxidation.

Tracking the morphology of the GUVs made of various unsaturated lipid compositions, we identified two consecutive stages upon illumination: a stage 1 in which the vesicles exhibit shape destabilizations, followed by a stage 2 associated with a rounding of the vesicles, decrease of their size and optical contrast, and occurrence of swell-burst cycles. Combining quantifications of these dynamic morphological changes and theoretical analysis, we estimated the decay of membrane permeability to sucrose with time. We further showed that the GUVs' lytic strain was decreased during the course of the illumination, pointing to a weakening of photooxidized membranes. Interestingly, we evidenced a complete absence of oxidation of the trans fatty chains. We showed that the onset of photooxidation is independent of the number of lipid unsaturation (18:1 and 18:2 GUVs) but is faster if the position of the unsaturation is close to the headgroup (18:1 Δ6-GUVs). However, the rate of optical contrast decay—related to the permeabilization of the membrane—is increased by both the number of double bonds and the proximity of the unsaturation to the headgroup. Interestingly, the permeabilization of the membrane is not proportional to its oxidation level and would be governed by a threshold effect.

To relate the dynamic morphological changes to the chemical processes occurring in situ during the photooxidation process, we conducted the RTM experiments on optically trapped LUVs. These Raman measurements allowed us to observe directly the long-scale kinetics, with time resolution of 3 s, of the following photoinduced processes: C=C bond isomerization, conjugation of C=C bonds, peroxide formation, and a cyclization reaction involving the six-membered ring structure.

Our findings shed light on the fundamental dynamic mechanisms underlying the oxidation of lipid membranes and highlight the role of unsaturations on their physical and chemical properties. This work has important implications in the understanding of organelles and cell membrane fate under oxidative stress and has the potential to help the development of preventive treatments against premature cell aging.

SUPPORTING MATERIAL

Supporting Materials and Methods, three figures, and one table are available at http://www.biophysj.org/biophysj/supplemental/S0006-3495(19)30083-9.

AUTHOR CONTRIBUTIONS

S.B. designed research. A.B., M.C., and S.G.K. performed research. M.C., P.R., and S.B. contributed analytic tools. A.B., S.G.K., N.P., and S.B. analyzed data. A.B., S.G.K., M.C., P.R., N.P., and S.B. wrote the manuscript.

ACKNOWLEDGMENTS

We thank C. Vever-Bizet and F. Sureau for helpful discussions.

We are grateful for financial support by Region Ile-de-France in the framework DIM Nano-K (S.B. and A.B.). M.C. and P.R. acknowledge the support of Office of Naval Research N00014-17-1- 2628 award.

REFERENCES

1. Assaly, R., Ad. de Tassigny, …, D. Morin. 2012. Oxidative stress, mitochondrial permeability transition pore opening and cell death during hypoxia-reoxygenation in adult cardiomyocytes. *Eur. J. Pharmacol.* 675:6–14.
2. Niki, E. 2008. Lipid peroxidation products as oxidative stress biomarkers. *Biofactors.* 34:171–180.
3. Dai, D. F., Y. A. Chiao, …, P. S. Rabinovitch. 2014. Mitochondrial oxidative stress in aging and healthspan. *Longev. Healthspan.* 3:6.
4. Halliwell, B. 2006. Oxidative stress and neurodegeneration: where are we now? *J. Neurochem.* 97:1634–1658.
5. Castano, A. P., T. N. Demidova, and M. R. Hamblin. 2005. Mechanisms in photodynamic therapy: part two-cellular signaling, cell metabolism and modes of cell death. *Photodiagn. Photodyn. Ther.* 2:1–23.
6. Dröge, W. 2002. Free radicals in the physiological control of cell function. *Physiol. Rev.* 82:47–95.
7. Sohal, R. S., R. J. Mockett, and W. C. Orr. 2002. Mechanisms of aging: an appraisal of the oxidative stress hypothesis. *Free. Radic. Biol. Med.* 33:575–586.
8. Kim, G. H., J. E. Kim, …, S. Yoon. 2015. The role of oxidative stress in neurodegenerative diseases. *Exp. Neurobiol.* 24:325–340.
9. Prasad, S., S. C. Gupta, …, L. Deb. 2016. Oxidative stress and cancer: advances and challenges. *Oxid. Med. Cell. Longev.* 2016:5010423.
10. Winklhofer, K. F., and C. Haass. 2010. Mitochondrial dysfunction in Parkinson's disease. *Biochim. Biophys. Acta.* 1802:29–44.
11. Moreira, P. I., C. Carvalho, …, G. Perry. 2010. Mitochondrial dysfunction is a trigger of Alzheimer's disease pathophysiology. *Biochim. Biophys. Acta.* 1802:2–10.
12. Zong, W. X., J. D. Rabinowitz, and E. White. 2016. Mitochondria and cancer. *Mol. Cell.* 61:667–676.
13. Sabharwal, S. S., and P. T. Schumacker. 2014. Mitochondrial ROS in cancer: initiators, amplifiers or an Achilles' heel? *Nat. Rev. Cancer.* 14:709–721.
14. Borst, J. W., N. V. Visser, …, A. J. Visser. 2000. Oxidation of unsaturated phospholipids in membrane bilayer mixtures is accompanied by membrane fluidity changes. *Biochim. Biophys. Acta.* 1487:61–73.
15. Runas, K. A., S. J. Acharya, …, N. Malmstadt. 2016. Addition of cleaved tail fragments during lipid oxidation stabilizes membrane permeability behavior. *Langmuir.* 32:779–786.

16. Runas, K. A., and N. Malmstadt. 2015. Low levels of lipid oxidation radically increase the passive permeability of lipid bilayers. *Soft Matter.* 11:499–505.

17. Buettner, G. R. 1993. The pecking order of free radicals and antioxidants: lipid peroxidation, alpha-tocopherol, and ascorbate. *Arch. Biochem. Biophys.* 300:535–543.

18. Agmon, E., J. Solon, …, B. R. Stockwell. 2018. Modeling the effects of lipid peroxidation during ferroptosis on membrane properties. *Sci. Rep.* 8:5155.

19. Garrec, J., A. Monari, …, M. Tarek. 2014. Lipid peroxidation in membranes: the peroxyl radical does not "float". *J. Phys. Chem. Lett.* 5:1653–1658.

20. Buettner, G. R., and B. A. Jurkiewicz. 1996. Catalytic metals, ascorbate and free radicals: combinations to avoid. *Radiat. Res.* 145:532–541.

21. Domingues, M. R., A. Reis, and P. Domingues. 2008. Mass spectrometry analysis of oxidized phospholipids. *Chem. Phys. Lipids.* 156:1–12.

22. Janero, D. R. 1990. Malondialdehyde and thiobarbituric acid-reactivity as diagnostic indices of lipid peroxidation and peroxidative tissue injury. *Free Radic. Biol. Med.* 9:515–540.

23. Karatekin, E., O. Sandre, …, F. Brochard-Wyart. 2003. Cascades of transient pores in giant vesicles: line tension and transport. *Biophys. J.* 84:1734–1749.

24. Paillous, N., and S. Fery-Forgues. 1994. Interest of photochemical methods for induction of lipid peroxidation. *Biochimie.* 76:355–368.

25. Baier, J., T. Maisch, …, W. Bäumler. 2006. Singlet oxygen generation by UVA light exposure of endogenous photosensitizers. *Biophys. J.* 91:1452–1459.

26. Bonneau, S., and C. Vever-Bizet. 2008. Tetrapyrrole photosensitisers, determinants of subcellular localisation and mechanisms of photodynamic processes in therapeutic approaches. *Expert Opin. Ther. Pat.* 18:1011–1025.

27. Dolmans, D. E., D. Fukumura, and R. K. Jain. 2003. Photodynamic therapy for cancer. *Nat. Rev. Cancer.* 3:380–387.

28. Kerdous, R., J. Heuvingh, and S. Bonneau. 2011. Photo-dynamic induction of oxidative stress within cholesterol-containing membranes: shape transitions and permeabilization. *Biochim. Biophys. Acta.* 1808:2965–2972.

29. Heuvingh, J., and S. Bonneau. 2009. Asymmetric oxidation of giant vesicles triggers curvature-associated shape transition and permeabilization. *Biophys. J.* 97:2904–2912.

30. Sankhagowit, S., S. H. Wu, …, N. Malmstadt. 2014. The dynamics of giant unilamellar vesicle oxidation probed by morphological transitions. *Biochim. Biophys. Acta.* 1838:2615–2624.

31. Mertins, O., I. O. Bacellar, …, R. Itri. 2014. Physical damage on giant vesicles membrane as a result of methylene blue photoirradiation. *Biophys. J.* 106:162–171.

32. Vyšniauskas, A., M. Qurashi, and M. K. Kuimova. 2016. A molecular rotor that measures dynamic changes of lipid bilayer viscosity caused by oxidative stress. *Chemistry.* 22:13210–13217.

33. Bouvrais, H., T. Pott, …, P. Méléard. 2010. Impact of membrane-anchored fluorescent probes on the mechanical properties of lipid bilayers. *Biochim. Biophys. Acta.* 1798:1333–1337.

34. Weber, G., T. Charitat, …, A. P. Schroder. 2014. Lipid oxidation induces structural changes in biomimetic membranes. *Soft Matter.* 10:4241–4247.

35. Kotova, E. A., A. V. Kuzevanov, …, Y. N. Antonenko. 2011. Selective permeabilization of lipid membranes by photodynamic action via formation of hydrophobic defects or pre-pores. *Biochim. Biophys. Acta.* 1808:2252–2257.

36. Mojzisova, H., S. Bonneau, …, D. Brault. 2009. Photosensitizing properties of chlorins in solution and in membrane-mimicking systems. *Photochem. Photobiol. Sci.* 8:778–787.

37. Mabrouk, E., S. Bonneau, …, P. Nassoy. 2010. Photosensitization of polymer vesicles: a multistep chemical process deciphered by micropipette manipulation. *Soft Matter.* 6:4863–4875.

38. Kuzelová, K., and D. Brault. 1994. Kinetic and equilibrium studies of porphyrin interactions with unilamellar lipidic vesicles. *Biochemistry.* 33:9447–9459.

39. Angelova, M., and D. S. Dimitrov. 1988. A mechanism of liposome electroformation. *In* Trends in Colloid and Interface. V. Degiorgio, ed. Steinkopff, pp. 59–67.

40. Bonneau, S., C. Vever-Bizet, …, D. Brault. 2007. Tetrapyrrole-photosensitizers vectorization and plasma LDL: a physico-chemical approach. *Int. J. Pharm.* 344:78–87.

41. Bonneau, S., N. Maman, and D. Brault. 2004. Dynamics of pH-dependent self-association and membrane binding of a dicarboxylic porphyrin: a study with small unilamellar vesicles. *Biochim. Biophys. Acta.* 1661:87–96.

42. Kerdous, R., F. Sureau, …, S. Bonneau. 2015. Release kinetics of an amphiphilic photosensitizer by block-polymer nanoparticles. *Int. J. Pharm.* 495:750–760.

43. Tatischeff, I., E. Larquet, …, S. G. Kruglik. 2012. Fast characterisation of cell-derived extracellular vesicles by nanoparticles tracking analysis, cryo-electron microscopy, and Raman tweezers microspectroscopy. *J. Extracell. Vesicles.* 1:19179.

44. Ashkin, A. 1970. Acceleration and trapping of particles by radiation pressure. *Phys. Rev. Lett.* 24:156–159.

45. Oglęcka, K., P. Rangamani, …, A. N. Parikh. 2014. Oscillatory phase separation in giant lipid vesicles induced by transmembrane osmotic differentials. *Elife.* 3:e03695.

46. Su, W. C., D. L. Gettel, …, A. N. Parikh. 2018. Pulsatile gating of giant vesicles containing macromolecular crowding agents induced by colligative nonideality. *J. Am. Chem. Soc.* 140:691–699.

47. Chabanon, M., J. C. S. Ho, …, P. Rangamani. 2017. Pulsatile lipid vesicles under osmotic stress. *Biophys. J.* 112:1682–1691.

48. Nomura, F., M. Nagata, …, K. Takiguchi. 2001. Capabilities of liposomes for topological transformation. *Proc. Natl. Acad. Sci. USA.* 98:2340–2345.

49. Chabanon, M., and P. Rangamani. 2018. Solubilization kinetics determines the pulsatory dynamics of lipid vesicles exposed to surfactant. *Biochim Biophys Acta Biomembr.* 1860:2032–2041.

50. Evans, E., and W. Rawicz. 1990. Entropy-driven tension and bending elasticity in condensed-fluid membranes. *Phys. Rev. Lett.* 64:2094–2097.

51. Rodriguez, N., J. Heuvingh, …, S. Cribier. 2005. Indirect evidence of submicroscopic pores in giant unilamellar [correction of unilamelar] vesicles. *Biochim. Biophys. Acta.* 1724:281–287.

52. Vamparys, L., R. Gautier, …, P. F. Fuchs. 2013. Conical lipids in flat bilayers induce packing defects similar to that induced by positive curvature. *Biophys. J.* 104:585–593.

53. Van der Paal, J., E. C. Neyts, …, A. Bogaerts. 2016. Effect of lipid peroxidation on membrane permeability of cancer and normal cells subjected to oxidative stress. *Chem. Sci.* 7:489–498.

54. Haluska, C. K., M. S. Baptista, …, R. Itri. 2012. Photo-activated phase separation in giant vesicles made from different lipid mixtures. *Biochim. Biophys. Acta.* 1818:666–672.

55. Muik, B., B. Lendl, …, M. J. Ayora-Cañada. 2005. Direct monitoring of lipid oxidation in edible oils by Fourier transform Raman spectroscopy. *Chem. Phys. Lipids.* 134:173–182.

56. Czamara, K., K. Majzner, …, M. Baranska. 2015. Raman spectroscopy of lipids: a review. *J. Raman Spectrosc.* 46:4–20.

57. Guo, Y., V. A. Baulin, and F. Thalmann. 2016. Peroxidised phospholipid bilayers: insight from coarse-grained molecular dynamics simulations. *Soft Matter.* 12:263–271.

58. Lee, H., and N. Malmstadt. 2018. Effect of low levels of lipid oxidation on the curvature, dynamics, and permeability of lipid bilayers and their interactions with cationic nanoparticles. *J. Phys. D Appl. Phys.* 51:164002.